

Machine learning clustering technique applied to powder X-ray diffraction patterns to distinguish alloy substitutions

Keishu Utimula¹, Rutchapon Hunkao², Masao Yano³, Hiroyuki Kimoto³,
Kenta Hongo^{4,5,6,9}, Shogo Kawaguchi⁷, Sujin Suwanna¹, Ryo Maezono^{8,9}

¹*School of Materials Science, JAIST,
Asahidai 1-1, Nomi, Ishikawa 923-1292, Japan*

²*Optical and Quantum Physics Laboratory,
Department of Physics, faculty of Science,
Mahidol University, Bangkok 10400, Thailand*

³*Advanced Material Engineering Div.,
Toyota Motor Corporation, Toyota-cho 1,
Toyota, Aichi 471-8572, Japan*

⁴*Research Center for Advanced Computing Infrastructure,
JAIST, Asahidai 1-1, Nomi, Ishikawa 923-1292, Japan*

⁵*Center for Materials Research by Information Integration,
Research and Services Division of Materials Data and Integrated System,
National Institute for Materials Science,
Tsukuba 305-0047, Japan*

⁶*PRESTO, JST, Kawaguchi, Saitama 332-0012, Japan*

⁷*Japan Synchrotron Radiation Research Institute (JASRI) Sayo-gun,
Hyogo 679-5148, Japan*

⁸*School of Information Science,
Japan Advanced Institute of Science and Technology (JAIST),
Asahidai 1-1, Nomi, Ishikawa 923-1292, Japan*

⁹*Computational Engineering Applications Unit, RIKEN,
2-1 Hirosawa, Wako, Saitama 351-0198, Japan*

We applied the clustering technique using DTW (dynamic time wrapping) analysis to XRD (X-ray diffraction) spectrum patterns in order to identify the microscopic structures of substituents introduced in the main phase of magnetic alloys. The clustering is found to perform well to identify the concentrations of the substituents with successful rates (~90%). The sufficient performance is attributed to the nature of DTW processing to filter out irrelevant informations such as the peak intensities (due to the incontrollability of diffraction conditions in polycrystalline samples) and the uniform shift of peak positions (due to the thermal expansions of lattices). The established framework is applicable not limited to the system treated in this work but widely to the systems to be tuned their properties by atomic substitutions within a phase. The framework has larger potential to predict wider properties from observed XRD patterns in a way that it can provide such properties evaluated from predicted microscopic local structure, such as magnetic moments, optical spectrum *etc.*).

I. INTRODUCTION

The concept of *materials informatics* based on the *big data science* has attracted recent interests in the context for discovering and exploring novel materials¹. Achieving high efficiency to get *data*, namely experimental measurements and analysis of materials, is necessary to accelerate the cycle of the exploration. XRD (X-ray diffraction) analysis is quite commonly used to capture crystal structures causing material properties². The analysis is getting accelerated by the improvements in X-ray intensities as well as in the environments of measurements³. Typical efforts to achieve efficiency in the analysis include such studies applying machine learn-

ing technique to series of XRD data in a systematic observation (*e.g.*, dependences on concentrations, temperature *etc.*) to extract significant information⁴. While materials informatics approaches combined with XRD data have been recently used to distinguish different phases (*i.e.*, *inter-phase* identifications)^{5–11}, no attempt has been made to tackle *intra-phase* ones so far. Along this context, the present study aims to provide a framework which can predict the concentrations of atomic substituents introduced in the main phase of polycrystalline magnetic alloys.

ThMn₁₂-type (Fig. 1) crystal structured SmFe_{11-x}Ti_x has been regarded as one of the candidates of the main phase in rare-earth permanent magnets¹². The origin of intrinsic prop-

erties emerging at high temperature as well as that of the phase stability has not yet been clarified well. Introducing Ti and Zr to substitute Fe and Sm is found to improve the magnetic properties and the phase stability, as described in details in Sec. 'Samples and experiments'. To clarify the mechanism how the substitutions improve the properties, it is desirable to identify substituted sites and its amount quantitatively, preferably with high throughput efficiency for accelerating the materials tuning. In this work, we have developed a machine learning clustering technique to distinguish powder XRD patterns to get such microscopic identifications about the atomic substitutions.

Ab initio calculations are used to generate supervising references for the machine learning of XRD patterns: We prepared several possible model structures with substituents located on different sites over a range of substitution fractions. Geometrical optimizations for each model give slightly different structures from each other. Then we generated many XRD patterns calculated from each structure. We found that the DTW (dynamic time wrapping) analysis can capture slight shifts in XRD peak positions corresponding to the differences of each relaxed structure, distinguishing the fractions and positions of substituents. We have established such a clustering technique using Ward's analysis on top of the DTW, being capable of sorting out simulated XRD patterns based on the distinction.

The established technique can hence learn the correspondence between XRD peak shifts and microscopic structures with substitutions over many supervising simulated data. Since the *ab initio* simulation can also give several properties such as magnetization for each structure, the correspondence in the machine learning can further predict functional properties of materials when it is applied to the experimental XRD patterns, not only being capable of distinguishing the atomic substitutions. The machine learning technique for XRD patterns developed here has therefore the wider range of applications not limited only on magnets, but further on those materials which properties are tuned by the atomic substitutions.

II. RESULTS

For our target system, $[\text{Sm}_{(1-y)}\text{Zr}_y]\text{Fe}_{12-x}\text{Ti}_x$, we examined the range for x and y as shown in Table I, which is accessible by the experiments. For a given concentration, several possible configurations for substituents exist. They are sorted into identical subgroups in terms of the crystalline symmetries, as described in Sec. 'Computational details'. Table. II and III summarize the possible space groups of substituted alloy structure (used as initial structures for computations) for given concentrations of Sm/Zr and Fe/Ti, respectively.

After applying lattice relaxations to the initial structures achieved by *ab initio* geometrical optimizations, we can calculate XRD patterns for the lattices. The procedures in details for the above are given in Sec. 'Computational details'. We could therefore generate 'simulated XRD patterns' as above, e.g., 26 patterns for the Sm/Zr substitution, those are the data for the clustering by the unsupervised learning. We examine

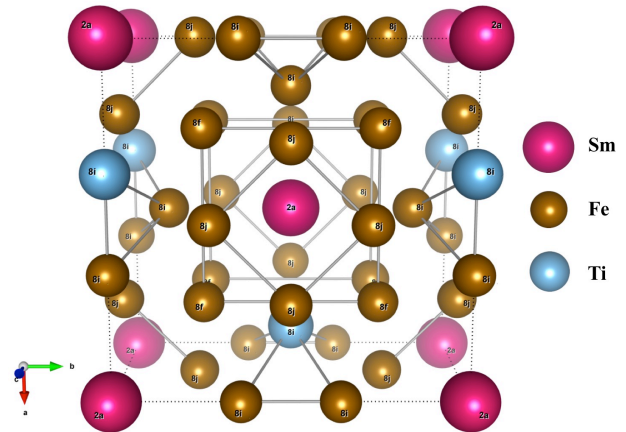


FIG. 1. The tetragonal ($Imm2$) crystal structure of $\text{SmFe}_{11}\text{Ti}$. Note that the labels are Wyckoff sites of space group before substitution by Ti ($I4/mmm$).

TABLE I. The numbers of inequivalent configurations of $\text{Sm}_{(1-y)}\text{Zr}_y\text{Fe}_{12-x}\text{Ti}_x$ to be considered. The numbers in bracket indicate the structure constructed from $2 \times 2 \times 2$ supercell (Sm/Zr), while the rest from $2 \times 2 \times 1$ supercell (Fe/Ti).

$y \backslash x$	0.0	0.5	1.0	1.5	2.0
0.000	1	13	22 (1)	27	61
0.125	-	-	(2)	-	-
0.250	-	-	(7)	-	-
0.375	-	-	(6)	-	-
0.500	-	-	(10)	-	-

whether the clustering can sort them again correctly based on their concentration.

Resultant XRD patterns (simulated one) fairly well coincides with experimental ones, as shown in Fig. 2. We see that the patterns keep the overall shape almost completely, just with slight variations in the inter-peak distances depending on the concentrations. To capture only such slight variations, DTW is expected to perform well due to the following reason: The method is designed to be applied to such signals given along an axis (e.g., time dependent signal, $y(t)$) so that it can extract only the *shape* of the signal ignoring uniform shifts along the axis. The method scores the *dissimilarity* between signals, i and j , in terms of the DTW-distance, $\text{DTW}(i, j)$.

Specifying a clustering framework is generally given by a combination of methods, $a \otimes b$, where 'a/that scoring the dissimilarity', and 'b/that making linkages between elements to form clusters based on the given dissimilarity'. In the present work, we employed the framework, [Normalized Constrained DTW (NC-DTW)] \otimes [Ward linkage method], using those implemented in 'Scipy package'¹³. The descriptions of linkage and dissimilarity-measure methods being used in this work can be found on the Scipy documents, except the DTW dissimilarity measures which were calculated by fastDTW¹⁴

TABLE II. [table.SmZr] Space groups of the initial structures for the substitution models (Sm/Zr) at each concentration. For $y = 0.5$, for instance, inequivalent configurations of substituted sites amounts to six in total. The number given in parenthesis represents the number of degenerated configurations within each symmetry at the initial structures for further lattice relaxations. It amounts therefore 26 configurations in total for generating simulated XRD patterns.

y (space group/number of configurations)				
0.000	0.125	0.250	0.375	0.500
<i>Imm2</i> (1)	<i>Imm2</i> (2)	<i>Amm2</i> (4)	<i>Imm2</i> (2)	<i>Imm2</i> (1)
		<i>Cmm2</i> (2)	<i>Cm</i> (2)	<i>Ima2</i> (2)
		<i>PI</i> (1)	<i>C2</i> (2)	<i>Cm</i> (2)
			<i>C2</i> (2)	<i>Pmm2</i> (2)
			<i>PI</i> (1)	

TABLE III. Space group of $\text{SmFe}_{12-x}\text{Ti}_x$ with inequivalent site of Ti substitutions. The $\text{SmFe}_{12}(\text{I4}/\text{mmm})$ is used as an initial structure. The number given in parenthesis represents the number of degenerated configurations within each symmetry at the initial structures for further lattice relaxations. It amounts therefore 124 configurations in total for generating simulated XRD patterns.

x (space group/number of configurations)				
0.0	0.5	1.0	1.5	2.0
<i>I4/mmm</i> (1)	<i>Cm</i> (1)	<i>Imm2</i> (2)	<i>Cm</i> (2)	<i>Fmmm</i> (2)
	<i>C2</i> (4)	<i>C2/m</i> (12)	<i>C2</i> (8)	<i>Immm</i> (4)
	<i>P-1</i> (8)	<i>C2/c</i> (6)	<i>P-1</i> (16)	<i>Fmm2</i> (1)
		<i>Cm</i> (1)	<i>PI</i> (1)	<i>Imm2</i> (1)
		<i>PI</i> (1)		<i>C2/m</i> (20)
				<i>C2/c</i> (4)
				<i>Cm</i> (4)
				<i>Cc</i> (1)
				<i>C2</i> (8)
				<i>P-1</i> (14)
				<i>PI</i> (2)

package. The framework is found to achieve the clustering to distinguish the concentration of Sm/Zr substitutions with sufficiently high accuracy, 96.2% (one failures among 26 XRD patterns), as shown in Fig. 3.

III. DISCUSSIONS

A. Limitation of the DTW-dissimilarity

When the same method (Ward \otimes DTW) as in Sm/Zr case is applied to Fe/Ti, the successful rate for the recognition gets reduced to 33.1%. We can identify the reason why the successful rate for the Fe/Ti gets worse than that for Sm/Zr from the dependence shown in Fig. 4. Since XRD reflects lattice constants as its peak position, we can take the unit cell volume, v , as a representative quantity to be captured by the clustering recognition under such a situation where the cell symmetry is kept unchanged. DTW dissimilarity, $\text{DTW}(i, j)$, can then

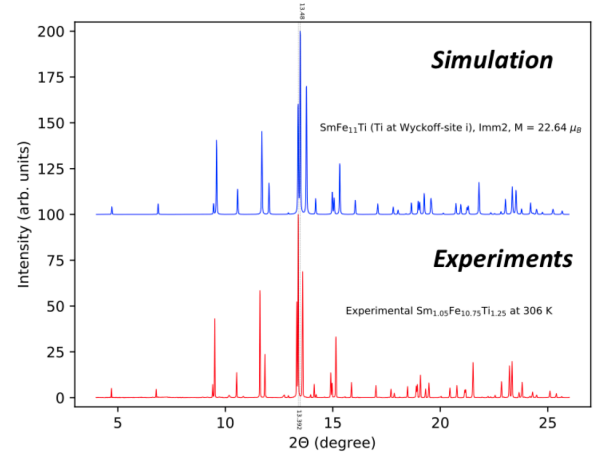


FIG. 2. Comparison of simulated XRD patterns (bottom) of $\text{SmFe}_{11}\text{Ti}$ and experimental XRD patterns (top) of $\text{Sm}_{1.05}\text{Fe}_{10.75}\text{Ti}_{1.25}$. The inset numbers are the main-phase peak position.

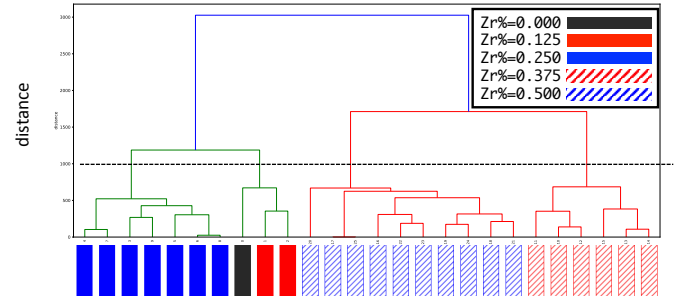


FIG. 3. Clustering over the XRD peak patterns (26 in total) of $[\text{Sm}_{1-y}\text{Zr}_y]\text{Fe}_{11}\text{Ti}$, performed by DTW (dynamical-time-wrapping) scoring and Ward linkage method. Putting the threshold around 1,000 for the dissimilarity (horizontal broken line), the patterns are clustered into four groups, sharing almost the same number of the substitutions by Zr. The red arrows at the bottom show the errors where a 'zero substitution' is wrongly sorted into the group with 'one substitution' etc.

be regarded to be scaling roughly to the difference of v . The recognition can therefore be regarded as such a framework to perform an *inverse inference* from the 'difference of v ' to identify the 'difference of x ' on the dependence of $v(x)$, as shown in Fig. 4. For Sm/Zr, the 'trace back mapping' from v to x is one-to-one, while for Fe/Ti it is not the case due to the *degeneracy* in the sense that many different values of v share the same x . Under such a *degeneracy*, it is impossible to provide correct inferences of 'difference in x ' from a given 'difference in v '. Such a difficulty occurring for the Fe/Ti case leads to the worse successful rate for the clustering recognition.

The problem can be resolved by a way assisted by the advantage of *ab initio* methods in the sense that they can provide

several other quantities not only the optimized lattice parameters. Even when $DTW(i, j) \sim |v(x_i) - v(x_j)|$ does not work well due to the degeneracy in $v(x)$, other quantities such as the magnetization $M(v)$ can be non-degenerate (as shown in Fig. 5) and hence useful to solve the difficulty. Using magnetizations is especially practical because the quantity is available from both experiments and simulations. We also note that the dependence in Fig. 4 (left panel) is consistent with the experimental fact¹⁵ that the magnetization per volume is increasing as the Zr concentration increases.

$$\text{Dissimilarity}(i, j) = \text{DTW}(i, j) \times W(i, j), \quad (1)$$

so that it can prevent from the problem due to the degeneracy. We have confirmed that the successful rate is actually improved from 33.1% into 99.19%, as shown in Fig. 6, by using the weight as above.

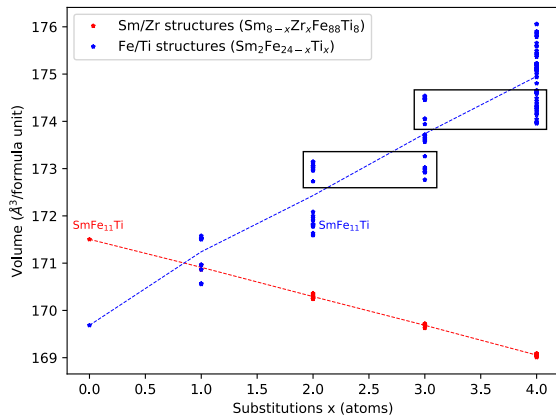


FIG. 4. Dependences of the unit cell volume (v) on the concentration x for Fe/Ti (blue) and Sm/Zr (red) substitutions. Several plots with the same color on the same x has the different symmetries as given in Table II and III. Rectangular enclosures on the blue dependence show the *degeneracy*, i.e., the different x may give the same v .

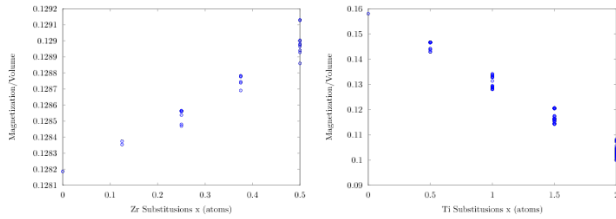


FIG. 5. Magnetizations depending on the concentrations for Sm/Zr ($\text{Sm}_{8-x}\text{Zr}_x\text{Fe}_{88}\text{Ti}_8$) [left panel] and Fe/Ti structures ($\text{Sm}_2\text{Fe}_{24-x}\text{Ti}_x$) [right panel].

B. How to treat experimental XRD

As shown in Fig. 2, simulated XRD patterns (s) well reproduce the experimental ones (e). The consistency is sufficiently

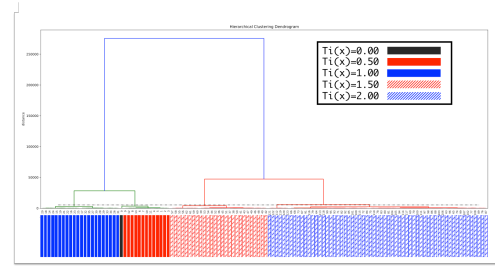


FIG. 6. Clustering over the XRD peak patterns (124 in total) of $\text{SmFe}_{12-x}\text{Ti}_x$, performed by DTW (dynamical-time-wrapping) scoring and Ward linkage method. The weighted function calculated from magnetization was used to improve the dissimilarity measures.

enough so that the *direct* comparison to evaluate the DTW distance, $DTW(e, s)$, can make sense for the clustering (it is usual that some pre-processing for law data, 'e' or 's', to get corrections, 'ē' or 's̄' to evaluate $DTW(\tilde{e}, \tilde{s})$ in order to fill the gap between the idealized simulations and realities). By preparing simulated XRDs, $(\{s_j\}_{j=1}^N)$, in advance, we can identify such a s_k for a given e which gives the smallest distance, $|e - s_k|$. The simulated s_k is accompanied by several quantities, $\{q_\alpha\}$, such as the formation energy, the magnetization, and the local geometrical configuration of substituents, those evaluated by *ab initio* method. Then the $\{q_\alpha\}$ can be the theoretical predictions for the observed e , serving a machine-learning framework for XRD patterns assisted by *ab initio* simulations. Fig. 7

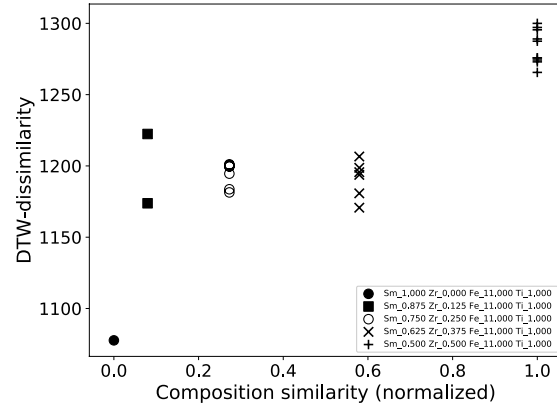


FIG. 7. DTW-dissimilarities between an experimental XRD (e) and simulated XRDs ($\{s_j\}$), being in a correlation with the composition similarity. The e is taken at the composition, $\text{Sm}_{1.05}\text{Zr}_{0.0}\text{Fe}_{10.75}\text{Ti}_{1.25}$, compared with $\{s_j\}$ in terms of $DTW(e, s_j)$ (vertical variable). The horizontal variable is the normalized 'composition similarity' defined by Eq. (2).

shows that such a distance, $|e - s_k|$, works fairly well, taking an example of e at a composition $\text{Sm}_{1.05}\text{Zr}_{0.0}\text{Fe}_{10.75}\text{Ti}_{1.25}$. For the general composition, $\text{Sm}_{c_1}\text{Zr}_{c_2}\text{Fe}_{c_3}\text{Ti}_{c_4}$, we can define the

'composition similarity' between e and $\{s_j\}$ as,

$$D = \sum_{\alpha=1}^4 (c_{\alpha}^{(e)} - c_{\alpha}^{(s)})^2. \quad (2)$$

In Fig. 7, we see that $\text{DTW}(e, s_j)$ (vertical variable) well correlates with the 'composition similarity'. The closest s_k giving the shortest $\text{DTW}(e, s_k)$ (black filled circle in the figure) has actually the closest composition, $\text{Sm}_{1.0}\text{Zr}_{0.0}\text{Fe}_{11.0}\text{Ti}_{1.0}$ than the other $\{s_j\}$. The prediction accuracy is simply improved by the more number of simulation data, $(\{s_j\}_{j=1}^N)$. A straightforward way to do so is to take more dense grid on x but it requires larger supercell and hence more computational power. For the present grid resolution, the experimental XRD with $\text{Zr}\%$ = 0.0, 10.4, and 31.8 are identified to be closest to $\text{Zr}\%$ (simulated) = 0, 25, and 37.5, respectively, being the best performance as possible.

In the case with the degeneracy (Fig. 4 for Fe/Ti substitution), the DTW distance is not capable of performing the clustering for $\{s_j\}$, and hence quite unlikely to be capable of identifying the closest s_k for a given e based on the $|e - s_k|$. The strategy with $W(i, j)$ (the weight by the magnetization) introduced in the previous section won't work in this case because for e (experimental XRD patterns), the accompanying quantities such as magnetizations are not always available. A possible remedy to distinguish e would be as follows using a plucked set, $\tilde{A} \subset A = \{s_j\}$: Since A is generated by simulations, each element is accompanied with the quantities like the magnetization, the formation energy *etc.*. By using the formation energies, we can pluck the degenerating candidates (e.g., P and Q in Fig. 8) by excluding ones with higher energies (P in Fig. 8) to form the plucked subset \tilde{A} . The degeneracy is now excluded in \tilde{A} , and hence used as a pool of references to be identified as the closest s_k to a given e based on the DTW distance, $|e - s_k|$. The identified s_k is accompanied with the physical quantities evaluated by the simulations, and hence they could be the estimates for the sample giving the experimental XRD, e .

C. Significance to use DTW

Clustering package 'Scipy'¹³ used here includes several other algorithms than our DTW \otimes Ward choice. It is worth interesting to see the comparisons of their performance, as shown in Table. IV-V with detailed explanations given in §VI.D. Although the NC-DTW does not show the best performance there, however, the compromise to the peak-shift of NC-DTW is required when we consider to treat experimental data. We note that the simulated XRDs are reflecting structures at zero temperature while the experimental ones are subject to thermal effects under the finite temperature. The effects would lead the broadening of peaks due to the thermal vibrations as well as the peak shifts due to the thermal expansions. Since we are looking at the change within a phase (not inter-phase changes), the shifts are expected to be almost

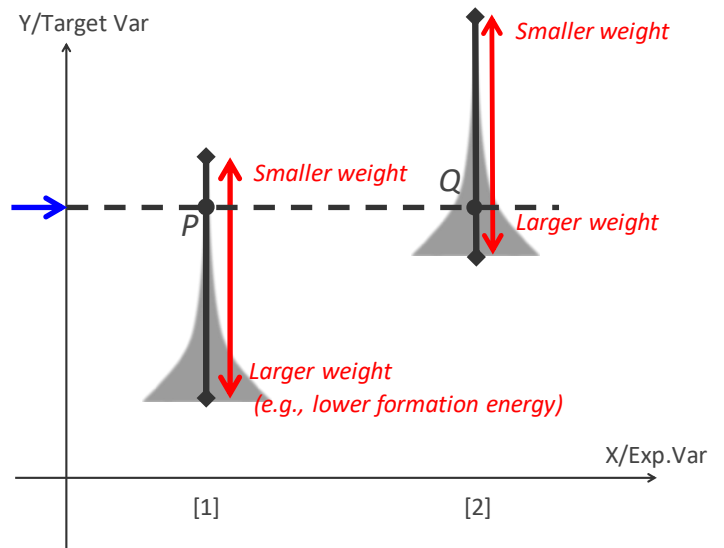


FIG. 8. A schematic picture explaining the difficulty to make proper distinctions in the clustering due to the 'degeneracy'. The horizontal axis corresponds to the substitution concentrations in our case, while the vertical one to the lattice parameters those characterize a XRD pattern. The 'errorbar-like' symbols represent the data spreading along the vertical axis shown in Fig. 4. When a XRD pattern is given as a point on the vertical axis (blue arrow), several points (P and Q) correspond to it with almost the same lattice parameters but with different internal alignments of defects, leading to the difficulty to mix up the possibilities of [1] and [2] as the possible 'explanation variable (concentration in this case)'. Red arrows beside the 'error-bars' mean that there is the weight, such as the formation energy, being possible to put over the spreading.

uniform, not so modifying the inter-peak distances significantly because the expansion occurs almost evenly for every lattice degrees of freedom. Such uniform shifts are not detected by DTW as its intention of the design, and hence the scoring works well not affected by the thermal effect. This nature forms the robustness against thermal noises on the experimental data enabling the direct comparison with simulation data at zero temperature to evaluate $|e - s_k|$. Based on the above observations, we positively use DTW even though it does not achieve the best performance for simulated data as seen in Table. IV-V. The evidence for this issue has also been shown in the preceding study⁷ as NC-DTW shows the best performance, among various techniques, to sort out the various phases from experimental data.

Several preceding works are found those applied DTW to analyse XRD patterns^{7,16}. While these studies applied it to distinguish phases (*i.e.*, inter-phase works), the present study works on the *intra-phase* identifications. In the formers, DTW is used to distinguish *major* differences of peak positions those drastically occurring when the phase changes⁷. In this study, on the other hand, we clarified the new capability of DTW, namely, it can distinguish even far tiny changes of inter-peak distances those occurring within a target phase. By this capa-

bility, we can explore a new framework that enables to identify the microscopic geometries of the substituents introduced in a target phase assisted by machine learning technique.

IV. CONCLUSION

We have developed such a clustering framework that can be applied to XRD patterns of alloys to distinguish the concentrations of substituents. We found that the clustering works quite well to identify the concentrations when applied to the patterns of magnetic alloys based on SmFe_{12} . Supercell models for the substitutions are found to work well with *ab initio* lattice relaxations, reproducing XRD patterns being sufficiently in coincidence with experiments. The implementation of the clustering with [DTW dissimilarity scoring]⊗ [Ward linkage method] is found to achieve around 90% of the successful rate for distinguishing the concentration. The main reason of the failure case in the clustering is identified being due to the *degeneracy*, namely the situation where different concentrations give almost the same lattice constant. By imposing quantities predicted by *ab initio* methods into the weight used for the dissimilarity scoring, such degeneracies are lifted to prevent the clustering from failure. Sufficiently good coincidence between simulated and experimental XRD patterns enables the framework to be used to predict unknown concentrations of the substituent introduced in the main phase of alloys from their XRD patterns. The established framework here is applicable not only to the system treated in this work but widely to the systems to be tuned their properties by atomic substitutions within a phase. Not only identifying the concentrations, the framework has larger potential for usefulness to predict wider properties from observed XRD patterns in a way that it can provide such properties evaluated from predicted microscopic local structure (positions of substitutions *etc.*), including magnetic moments, optical spectrum *etc.*

V. ACKNOWLEDGMENTS

The computations in this work have been performed using the facilities of Research Center for Advanced Computing Infrastructure at JAIST. R.M. is grateful for financial supports from MEXT-KAKENHI (17H05478 and 16KK0097), from FLAGSHIP2020 (project nos. hp180206 and hp180175 at K-computer), from Toyota Motor Corporation, from I-O DATA Foundation, and from the Air Force Office of Scientific Research (AFOSR-AOARD/FA2386-17-1-4049). K.H. is grateful for financial supports from FLAGSHIP2020 (project nos. hp180206 and hp180175 at K-computer), KAKENHI grant (17K17762), a Grant-in-Aid for Scientific Research on Innovative Areas (16H06439), PRESTO (JPMJPR16NA) and the “Materials research by Information Integration Initiative” (MI²I) project of the Support Program for Starting Up Innovation Hub from Japan Science and Technology Agency (JST). R.H. is grateful for financial support from the Development and Promotion of Science and Technology Talents Project

(DPST) for a scholarship to study at Faculty of Science, Mahi-dol University, and research internship at JAIST.

VI. SUPPLEMENTAL INFORMATION

A. Samples and Experiments

The X-ray diffraction (XRD) measurements for the powdered Sm-Fe-Ti were performed at the beamline BL02B2 in SPring-8 (Proposal Nos. 2016B1618 and 2017A1602). CeO_2 diffraction pattern was used to determine the X-ray energy of 25 keV. The diffraction intensities were collected using a sample rotator system and a high-resolution one-dimensional semiconductor detector (multiple MYTHEN system) with a step size of $2\theta = 0.006$ [deg.]³. The samples were powdered from strip-casted alloys and the powder was put into a quartz capillary and encapsulated with negative pressure of Ar gas.

B. Computational Details

For getting the structures of the target alloys, $[\text{Sm}_{(1-y)}\text{Zr}_y]\text{Fe}_{12-x}\text{Ti}_x$, we firstly constructed a tetragonal ($I4/mmm$) crystal structure of SmFe_{12} using experimental lattice parameters, $a = 0.856$ nm and $b = 0.480$ nm ($b = a$), of $\text{SmFe}_{11}\text{Ti}$ ¹⁷ as an initial setting for further optimizations. For Zr-substitutions replacing Sm sites (ranging from 1-4 atoms), we constructed $2 \times 2 \times 2$ supercell, containing 104 atoms in the primitive of tetragonal ($Imm2$) of $\text{SmFe}_{11}\text{Ti}$ (Fig. 1). All possible configurations were considered to cover a randomness of experimental substitutions, and we ignored some configurations by considering their symmetry using FINDSYM software¹⁸. Finally, we considered only 26 supercells (Table. II) that possess different space groups, Wyckoff site occupations.

For *ab initio* calculations, we used the spin-polarized density functional theory (DFT) implemented in the ‘Vienna *ab initio* simulation package (VASP)’^{19–21}. For such systems like our target those including transition metal and rare earth elements, it is generally known that the predictions are critically influenced by the choice of exchange-correlation (XC) potentials used in DFT^{22–25}. For the present case, it has been found that DFT+*U* is essentially inevitable if we treat *f*-orbitals as the valence range^{26–30}. It has also been found that GGA (generalized gradient approximation) works well if the $4f$ is treated as the core range described by pseudo potentials^{31–35}. We therefore used the revised Perdew-Burke-Erzenhof (RPBE)³⁶ for the GGA-XC upon the confirmation that RPBE improves optimized lattice parameters getting closer to experiment ones than when PBE³⁷ used. The pseudopotentials based on projected augmented wave (PAW)³⁸ method were used. The *s* and *p* semi-core states are included in valence states, except Sm, resulting in 12, 16 and 12 valence states for Zr, Fe and Ti, respectively. The structural relaxations were done until a force on each ion was smaller than 0.01 eV \AA^{-1} . A plane-wave cutoff energy of 400 eV and $5 \times 5 \times 5$ Monkhorst-Pack grids

were used which was large enough to give convergence energy. The lattice relaxations with the above choice applied to $\text{SmFe}_{11}\text{Ti}$ is confirmed to get the lowest total energy with Ti at 8i site, which is consistent with experiments^{12,39} and *ab initio* calculations⁴⁰ of RFe_{11}Ti -type magnetic compounds. The optimized lattice parameters, a and c , were 0.851 and 0.473 [nm] which are good agreement with the experiments¹⁷ These comparisons confirm that our model sufficiently reasonable. With Ti substitution at 8i site, $I4/mmm$ space group breaks and becomes $Imm2$ as shown in Fig. 1.

C. Validation of simulated XRD patterns

To validate our simulated XRD pattern, the simulated XRD patterns were compared to the experimental XRD patterns. The X-ray diffraction (XRD) patterns of the optimized structures were theoretically calculated by the powder diffraction pattern utility in VESTA⁴¹ software. The X-ray wavelength of 0.496 Å was used as being used in experiment. The isotropic atomic displacement parameter (B) was set to 1.00 Å. The normalized XRD patterns having 2θ from 1 to 120 degree with 0.01 degree interval was obtained.

The simulated XRD pattern of $\text{SmFe}_{11}\text{Ti}$ agrees very well with the experimental XRD pattern of $\text{Sm}_{1.05}\text{Fe}_{10.75}\text{Ti}_{1.25}$ (Fig. 2), but the main-phase peak position is quite different as it is 13.41 deg. in experiment while 13.48 deg. in simulation. This is due to the fact that the peak shift occurs if the lattice expands or contracts, and we found that the optimized lattice parameters from DFT are underestimated which accounts for the difference. This underestimated lattice parameters introduce only systematic shift of peak position but their XRD profiles remain unchanged. When the Zr concentration increases, the main-phase peak position of the simu-

lated XRD patterns shifts to larger 2θ , being in accordance with experimental results.

D. Hierarchical clustering analysis

The hierarchical clustering analysis (HCA) was used to identify the simulated XRD patterns. All clustering analysis were carried out using Scipy package¹³. The descriptions of linkage and dissimilarity-measure methods being used in this work can be found on the Scipy documents, except the DTW dissimilarity measures which were calculated by fastDTW¹⁴ package. The package provides variety of other methods than the present choice, DTW@Ward, as shown in Table IV-V. The tables compares the performances achieved by the variety of choices for the identifications of Sm/Zr and Fe/Ti, respectively. The performance is evaluated in terms of ARI (adjusted Rand index), which measures the similarity between the true labels and predicted labels with the maximum score and minimum score of 1 and -1, respectively. The ARI calculations have been done by using 'Scikit-learn' package⁴². In the tables, several dissimilarity measures, NC-DTW, Euclidean, Cityblock, Cosine and Correlation, with various linkage methods, Single, Complete, Average, Weighted, Centroid, Median and Ward, have been compared. The perfect score of 1 is reached by all methods, except NC-DTW, in Sm/Zr structures. While the best method in Fe/Ti structures are cosine and correlation with ward linkage with 0.55 score. The NC-DTW method provides lower performance than other methods in both structures since the NC-DTW omits the peak-shift information while the rest are peak-position based dissimilarity measure. With NC-DTW dissimilarity measure, the ward linkage method shows the a good performance, ARI of 0.91 and 0.01 for Sm/Zr and Fe/Ti structures, respectively, among all linkage methods. Therefore, in this work, we will focus on NC-DTW with ward linkage method.

-
- ¹ H. Ikebata, K. Hongo, T. Isomura, R. Maezono, and R. Yoshida, *Journal of computer-aided molecular design* **31**, 379 (2017).
 - ² K. Hongo, S. Kurata, A. Jomphoak, M. Inada, K. Hayashi, and R. Maezono, *Inorganic Chemistry* **57**, 5413 (2018), pMID: 29658713, <https://doi.org/10.1021/acs.inorgchem.8b00381>.
 - ³ S. Kawaguchi, M. Takemoto, K. Osaka, E. Nishibori, C. Mori-yoshi, Y. Kubota, Y. Kuroiwa, and K. Sugimoto, *Review of Scientific Instruments* **88**, 085111 (2017), <https://doi.org/10.1063/1.4999454>.
 - ⁴ W. B. Park, J. Chung, J. Jung, K. Sohn, S. P. Singh, M. Pyo, N. Shin, and K.-S. Sohn, *IUCrJ* **4**, 486 (2017).
 - ⁵ A. G. Kusne, T. Gao, A. Mehta, L. Ke, M. C. Nguyen, K.-M. Ho, V. Antropov, C.-Z. Wang, M. J. Kramer, C. Long, and I. Takeuchi, *Scientific Reports* **4**, 6367 (2014), article.
 - ⁶ S. K. Suram, Y. Xue, J. Bai, R. Le Bras, B. Rappazzo, R. Bernstein, J. Bjorck, L. Zhou, R. B. van Dover, C. P. Gomes, and J. M. Gregoire, *ACS Combinatorial Science* **19**, 37 (2017), pMID: 28064478, <https://doi.org/10.1021/acscombsci.6b00153>.
 - ⁷ Y. Iwasaki, A. G. Kusne, and I. Takeuchi, *npj Computational Materials* **3**, 4 (2017).
 - ⁸ S. Li, Z. Xiong, and J. Hu, *Materials Science and Technology* **34**, 315 (2018), <https://doi.org/10.1080/02670836.2017.1389116>.
 - ⁹ V. Stanev, V. V. Vesselinov, A. G. Kusne, G. Antoszewski, I. Takeuchi, and B. S. Alexandrov, *npj Computational Materials* **4**, 43 (2018).
 - ¹⁰ H. Xing, B. Zhao, Y. Wang, X. Zhang, Y. Ren, N. Yan, T. Gao, J. Li, L. Zhang, and H. Wang, *ACS Combinatorial Science* **20**, 127 (2018), pMID: 29381327, <https://doi.org/10.1021/acscombsci.7b00171>.
 - ¹¹ C. Oses, E. Gossett, D. Hicks, F. Rose, M. J. Mehl, E. Perim, I. Takeuchi, S. Sanvito, M. Scheffler, Y. Lederer, O. Levy, C. Toher, and S. Curtarolo, *Journal of Chemical Information and Modeling* **58**, 2477 (2018), pMID: 30188699, <https://doi.org/10.1021/acs.jcim.8b00393>.
 - ¹² K. Kobayashi, S. Suzuki, T. Kuno, K. Urushibata, N. Sakuma, M. Yano, T. Shoji, A. Kato, and A. Manabe, *Journal of Magnetism and Magnetic Materials* **426**, 273 (2017).
 - ¹³ E. Jones, T. Oliphant, P. Peterson, *et al.*, "SciPy: Open source scientific tools for Python," (2001-).
 - ¹⁴ S. Salvador and P. Chan, *Intell. Data Anal.* **11**, 561 (2007).

TABLE IV. [table.score1]Adjusted rand index of clustering result of $\text{Sm}_{1-y}\text{Zr}_y\text{Fe}_{11}\text{Ti}$ (Sm/Zr) structures.

	Single	Complete	Average	Weighted	Centroid	Median	Ward
NC-DTW	1.00	0.80	1.00	0.82	0.82	0.82	0.91
Cityblock	1.00	1.00	1.00	1.00	1.00	1.00	1.00
Euclidean	1.00	1.00	1.00	1.00	1.00	1.00	1.00
Cosine	1.00	1.00	1.00	1.00	1.00	1.00	1.00
Correlation	1.00	1.00	1.00	1.00	1.00	1.00	1.00

TABLE V. [table.score2]Adjusted rand index of clustering result of $\text{SmFe}_{12-x}\text{Ti}_x$ (Fe/Ti) structures.

	Single	Complete	Average	Weighted	Centroid	Median	Ward
NC-DTW	-0.04	-0.10	-0.08	-0.08	-0.04	-0.04	0.01
Cityblock	-0.06	0.49	0.45	0.39	0.27	0.40	0.41
Euclidean	-0.03	0.28	0.47	0.49	0.27	0.28	0.28
Cosine	-0.01	0.35	0.51	0.55	0.33	0.28	0.35
Correlation	-0.01	0.34	0.51	0.55	0.33	0.33	0.35

- ¹⁵ T. Kuno, S. Suzuki, K. Urushibata, K. Kobayashi, N. Sakuma, M. Yano, A. Kato, and A. Manabe, *AIP Advances* **6**, 025221 (2016), <https://doi.org/10.1063/1.4943051>.
- ¹⁶ L. A. Baumes, M. Moliner, N. Nicoloyannis, and A. Corma, *CrystEngComm* **10**, 1321 (2008).
- ¹⁷ T. Kuno, S. Suzuki, K. Urushibata, K. Kobayashi, N. Sakuma, M. Yano, A. Kato, and A. Manabe, *AIP Advances* **6**, 025221 (2016), <https://doi.org/10.1063/1.4943051>.
- ¹⁸ H. T. Stokes and D. M. Hatch, *Journal of Applied Crystallography* **38**, 237 (2005).
- ¹⁹ G. Kresse and J. Hafner, *Phys. Rev. B* **47**, 558 (1993).
- ²⁰ G. Kresse and J. Furthmüller, *Computational Materials Science* **6**, 15 (1996).
- ²¹ G. Kresse and J. Furthmüller, *Phys. Rev. B* **54**, 11169 (1996).
- ²² K. Hongo and R. Maezono, *Journal of Chemical Theory and Computation* **13**, 5217 (2017), pMID: 28981266, <https://doi.org/10.1021/acs.jctc.6b01159>.
- ²³ T. Ichibha, Z. Hou, K. Hongo, and R. Maezono, *Scientific Reports* **7**, 2011 (2017).
- ²⁴ K. Hongo, M. A. Watson, T. Iitaka, A. Aspuru-Guzik, and R. Maezono, *Journal of Chemical Theory and Computation* **11**, 907 (2015), pMID: 26579744, <https://doi.org/10.1021/ct500401p>.
- ²⁵ K. Hongo, N. T. Cuong, and R. Maezono, *Journal of Chemical Theory and Computation* **9**, 1081 (2013), pMID: 26588751, <https://doi.org/10.1021/ct301065f>.
- ²⁶ P. Larson, I. I. Mazin, and D. A. Papaconstantopoulos, *Phys. Rev. B* **67**, 214405 (2003).
- ²⁷ S. Yehia, S. H. Aly, and A. E. Aly, *Computational Materials Science* **41**, 482 (2008).
- ²⁸ X. Liu and Z. Altounian, *Computational Materials Science* **50**, 841 (2011).
- ²⁹ H. Pang, L. Qiao, and F. S. Li, *physica status solidi (b)* **246**, 1345, <https://onlinelibrary.wiley.com/doi/pdf/10.1002/pssb.200844215>.
- ³⁰ W. Cheng, S. Zhao, X. Cheng, and X. Miao, *Journal of Superconductivity and Novel Magnetism* **25**, 1947 (2012).
- ³¹ Y. Harashima, K. Terakura, H. Kino, S. Ishibashi, and T. Miyake, *Journal of Applied Physics* **120**, 203904 (2016), <https://doi.org/10.1063/1.4968798>.
- ³² P. Larson, I. I. Mazin, and D. A. Papaconstantopoulos, *Phys. Rev. B* **69**, 134408 (2004).
- ³³ M. Duerrschnabel, M. Yi, K. Uestuener, M. Liesegang, M. Katter, H. J. Kleebe, B. Xu, O. Gutfleisch, and L. Molina-Luna, *Nature Communications* **8**, 54 (2017).
- ³⁴ A. Ismail, J. Hooper, J. B. Giorgi, and T. K. Woo, *Phys. Chem. Chem. Phys.* **13**, 6116 (2011).
- ³⁵ B. Puchala and A. Van der Ven, *Phys. Rev. B* **88**, 094108 (2013).
- ³⁶ B. Hammer, L. B. Hansen, and J. K. Nørskov, *Phys. Rev. B* **59**, 7413 (1999).
- ³⁷ J. P. Perdew, K. Burke, and M. Ernzerhof, *Phys. Rev. Lett.* **77**, 3865 (1996).
- ³⁸ G. Kresse and D. Joubert, *Phys. Rev. B* **59**, 1758 (1999).
- ³⁹ Y. chang Yang, X. dong Zhang, L. shu Kong, Q. Pan, S. lin Ge, J. lian Yang, Y. fan Ding, B. sheng Zhang, C. tang Ye, and L. Jin, *Solid State Communications* **78**, 313 (1991).
- ⁴⁰ Y. Harashima, K. Terakura, H. Kino, S. Ishibashi, and T. Miyake, *Phys. Rev. B* **92**, 184426 (2015).
- ⁴¹ K. Momma, F. Izumi, and IUCr, *Journal of Applied Crystallography* **44**, 1272 (2011).
- ⁴² F. Pedregosa, G. Varoquaux, A. Gramfort, V. Michel, B. Thirion, O. Grisel, M. Blondel, P. Prettenhofer, R. Weiss, V. Dubourg, J. Vanderplas, A. Passos, D. Cournapeau, M. Brucher, M. Perrot, and E. Duchesnay, *J. Mach. Learn. Res.* **12**, 2825 (2011).